AIAA SciTech Forum
12-16 January 2026, Orlando, FL
AIAA SCITECH 2026 Forum

10.2514/6.2026-1873

Toward resolvent-based estimation and control of wavepackets in supersonic turbulent jets

Yuhao Zhou*, Aaron Towne†
University of Michigan, Ann Arbor, MI 48109, USA

Junoh Jung‡
Argonne National Laboratory, Lemont, IL 60439, USA

Rutvij Bhagwat§
Florida State University, Tallahassee, FL 32310, USA

Eduardo Martini¶, Peter Jordan‖
Institut PPrime, CNRS–Université de Poitiers–ENSMA, 86000 Poitiers, France

Diego B.S. Audiffred**, Igor Maia††, André V. G. Cavalieri‡‡
Instituto Tecnológico de Aeronáutica, São José dos Campos, SP, Brazil

High-speed-jet turbulent mixing noise remains a challenging problem, and here we aim to reduce it using a wavepacket-cancellation strategy. This approach is enabled by the recently developed resolvent-based estimation and control framework, which uses near-nozzle sensors to detect noise-generating wavepackets and suppress them via actuation. This paper presents three main results toward this larger goal: (i) data-driven estimation for a Mach 1.5 supersonic jet using large-eddy simulations to identify coherent structures and inform sensor-target placement; (ii) resolvent-based estimation for the linearized jet, which achieves reasonable accuracy in reconstructing relevant flow features from limited sensor data; and (iii) preliminary resolvent-based control for the linearized jet, demonstrating a 34% reduction in the root mean square of streamwise-momentum fluctuations using only one sensor and one actuator. These findings demonstrate the potential of the resolvent-based framework for mitigating noise-generating wavepacket structures in supersonic jets and provide an important foundation for future computational and experimental investigations.

I. Introduction

Jet noise continues to challenge both commercial and military aviation sectors. Commercial aircraft with turbofan engines benefit from noise reduction through a high bypass ratio [1, 2], as jet noise is strongly correlated with plume velocity [3]. However, further reduction in noise through this method faces technical limitations, and this method cannot be applied to existing engine designs [4]. On the other hand, military aviation confronts greater difficulties, as operational requirements exclude high-bypass designs. This leads to hazardous noise levels (>140 dB) that endanger personnel and surrounding communities [5, 6]. As a result, the U.S. Department of Veterans Affairs' annual expenditure exceeds $1 billion on noise-induced hearing loss [7]. These persistent challenges highlight the critical need for innovative noise reduction strategies for turbulent jets.

*Graduate Student Research Assistant, Department of Mechanical Engineering
†Associate Professor, Department of Mechanical Engineering, AIAA Senior Member
‡Post-Doctoral Research Fellow, Mathematics and Computer Science Division
§Postdoctoral Scholar, Department of Mechanical Engineering
¶Professor, Département Fluides Thermique et Combustion
‖Professor, Département Fluides Thermique et Combustion
**Graduate Student, Division of Aeronautical Engineering
††Post-Doctoral Research Fellow, Département Aérodynamique, Énergétique et Propulsion
‡‡Professor, Division of Aeronautical Engineering

Jet noise mitigation strategies have historically followed two primary approaches. The first category involves passive control methods that modify the nozzle geometry or internal surfaces, including chevron nozzles [8–10], nozzle inserts [11–13], and lip roughness [14]. The second category comprises active flow control techniques designed to modify the flowfield using steady or periodic actuators, such as microjets [15–18] and plasma actuators [19–23]. While these methods demonstrate measurable effects, they achieve only modest noise reduction (on the order of a few dB) in practical applications. More recently, closed-loop control has gained attention as a promising approach for achieving greater noise reduction by detecting and canceling noise-generating wavepackets.

Our work is based on a series of work related to resolvent-based estimation and control. Schmidt et al. [24] showed that resolvent analysis is able to model large-scale wavepacket structures efficiently. Towne et al. [25] showed that resolvent analysis is a powerful tool for flow reconstruction, especially for high-speed jets with a large gain separation of resolvent modes. Furthermore, Towne et al. [26] showed that incorporating the statistics of the nonlinear forcing into resolvent analysis could effectively improve estimation results. Martini et al. [27, 28] extended the resolvent-based approach with optimal control methods to obtain non-causal optimal estimates, and achieved causality through Wiener-Hopf formalism [29]. Jung and Towne [30] applied these tools to estimate and control fluctuations in the laminar flow over an airfoil and to improve the lift force, and later extended the approach to turbulent wakes for flow estimation [31]. Towne et al. [32] used these tools to estimate wavepackets of a subsonic turbulent jet. Maia et al. [33] implemented a real-time feedforward control scheme on a forced turbulent jet, using upstream sensor measurements to attenuate axisymmetric wavepackets, achieving an order-of-magnitude reduction in velocity fluctuations. Audiffred et al. [34] advanced this approach by applying the Wiener-Hopf formalism to design optimal causal controllers for both forced and natural jets, leading to up to 60% attenuation in the power spectra of naturally occurring disturbances. In the context of installed jet noise, Audiffred et al. [35] demonstrated that reactive closed-loop control based on Wiener-Hopf theory significantly outperforms truncated-kernel methods, yielding up to 5 dB reduction in far-field noise caused by jet-surface interaction.

Our work focuses on leveraging recently developed resolvent-based tools within a compressible flow solver to estimate and control noise-generating wavepackets in supersonic jets. First, we perform large-eddy simulations (LES) of a Mach 1.5 jet. Data-driven estimation, based on sensor-target readings extracted from LES results, is employed to analyze the underlying wavepacket structures and inform sensor and target placement. Second, resolvent-based estimation is conducted to the linearized jet with external forcing modeled as white noise, to test and validate the resolvent-based tools under supersonic conditions and further guide the placement of sensors, actuators, and targets. Finally, closed-loop control is applied to the linearized jet to evaluate the effectiveness of the control framework.

The rest of the paper is structured as follows. The formulation of the resolvent-based estimation and control method, along with its numerical framework, is discussed in section II. The setup of a 1.5-Mach jet and data-driven estimation results are discussed in section III.A and III.B. The setup and results of resolvent-based estimation and control of the linearized jet are shown in section III.D and section III.E, respectively. Conclusions and future work are discussed in section IV.

II. Methods

A. System Definition

The resolvent-based estimation framework begins by casting the linearized Navier-Stokes equations as a linear time-invariant system,

$$\frac{d\boldsymbol{q}}{dt}(t) = \boldsymbol{A_q}(t) + \boldsymbol{B}_f\boldsymbol{f}(t) + \boldsymbol{B}_a\boldsymbol{a}(t), \tag{1a}$$

$$\boldsymbol{y}(t) = \boldsymbol{C}_y\boldsymbol{q}(t) + \boldsymbol{n}(t), \tag{1b}$$

$$\boldsymbol{z}(t) = \boldsymbol{C}_z\boldsymbol{q}(t), \tag{1c}$$

where $\boldsymbol{q} \in \mathbb{C}^n$ is the spatially-discretized state vector, $\boldsymbol{f} \in \mathbb{C}^{n_f}$ is the forcing term composed of nonlinear terms and external disturbances, $\boldsymbol{A} \in \mathbb{C}^{n\times n}$ is the linearized compressible Navier-stokes operator, $\boldsymbol{B}_f \in \mathbb{C}^{n\times n_f}$ specifies the spatial location and parameters of the nonlinear forcing, $\boldsymbol{a} \in \mathbb{C}^{n_a}$ is a vector of actuator signals, and $\boldsymbol{B}_a \in \mathbb{C}^{n\times n_a}$ specifies the spatial location and parameters of actuators. Sensor measurements $\boldsymbol{y} \in \mathbb{C}^{n_y}$ and target measurements $\boldsymbol{z} \in \mathbb{C}^{n_z}$ are extracted from the state vector $\boldsymbol{q}$ using $\boldsymbol{C}_y \in \mathbb{C}^{n_y\times n}$ and $\boldsymbol{C}_z \in \mathbb{C}^{n_z\times n}$, respectively, and $\boldsymbol{n}$ is the sensor measurement noise. Enabled by the linearity of the system Eq. (1) can be split into a forcing-driven system and an

actuation-driven system [29]. The forcing-driven system with sensor noise is

$$\frac{d\boldsymbol{q}_f}{dt}(t) = \boldsymbol{A}\boldsymbol{q}_f(t) + \boldsymbol{B}_f\boldsymbol{f}(t), \tag{2a}$$

$$\boldsymbol{y}_f(t) = \boldsymbol{C}_y\boldsymbol{q}_f(t) + \boldsymbol{n}(t), \tag{2b}$$

$$\boldsymbol{z}_f(t) = \boldsymbol{C}_z\boldsymbol{q}_f(t). \tag{2c}$$

The actuation-driven system is

$$\frac{d\boldsymbol{q}_a}{dt}(t) = \boldsymbol{A}\boldsymbol{q}_a(t) + \boldsymbol{B}_a\boldsymbol{a}(t), \tag{3a}$$

$$\boldsymbol{y}_a(t) = \boldsymbol{C}_y\boldsymbol{q}_a(t), \tag{3b}$$

$$\boldsymbol{z}_a(t) = \boldsymbol{C}_z\boldsymbol{q}_a(t). \tag{3c}$$

The full system can be recovered by adding the states, sensor, and target measurements of the two systems together,

$$\boldsymbol{q} = \boldsymbol{q}_f + \boldsymbol{q}_a, \tag{4a}$$

$$\boldsymbol{y} = \boldsymbol{y}_f + \boldsymbol{y}_a, \tag{4b}$$

$$\boldsymbol{z} = \boldsymbol{z}_f + \boldsymbol{z}_a. \tag{4c}$$

The Fourier transform of Eq. (2) and Eq. (3) yields the input-output relationships of sensor and target measurements with forcing and actuation signal, respectively,

$$\hat{\boldsymbol{y}}_f = \boldsymbol{R}_{yf}\hat{\boldsymbol{f}} + \hat{\boldsymbol{n}}, \tag{5a}$$

$$\hat{\boldsymbol{z}}_f = \boldsymbol{R}_{zf}\hat{\boldsymbol{f}}, \tag{5b}$$

$$\hat{\boldsymbol{y}}_a = \boldsymbol{R}_{ya}\hat{\boldsymbol{a}}, \tag{5c}$$

$$\hat{\boldsymbol{z}}_a = \boldsymbol{R}_{za}\hat{\boldsymbol{a}}. \tag{5d}$$

Here, $\boldsymbol{R}_{yf} = \boldsymbol{C}_y\boldsymbol{R}\boldsymbol{B}_f$, $\boldsymbol{R}_{zf} = \boldsymbol{C}_z\boldsymbol{R}\boldsymbol{B}_f$, $\boldsymbol{R}_{ya} = \boldsymbol{C}_y\boldsymbol{R}\boldsymbol{B}_a$ and $\boldsymbol{R}_{za} = \boldsymbol{C}_z\boldsymbol{R}\boldsymbol{B}_a$ are modified resolvent operators (sometimes called input-output operators), and $\boldsymbol{R} = (-i\omega\boldsymbol{I} - \boldsymbol{A})^{-1}$ is the resolvent operator.

B. Resolvent-based estimation

We define the estimated target value as an convolution of the estimation kernel and the sensor measurements [27],

$$\tilde{\boldsymbol{z}}(t) = \int_{-\infty}^{\infty} \boldsymbol{T}(t-\tau)\boldsymbol{y}(\tau)d\tau, \tag{6}$$

where $\boldsymbol{T} \in \mathbb{C}^{n_z \times n_y}$ is the estimation kernel, $\boldsymbol{y}$ is the sensor measurement, and $\tilde{\boldsymbol{z}}$ is the estimated target value. The Fourier transformation yields an equivalent expression in the frequency domain,

$$\hat{\tilde{\boldsymbol{z}}} = \hat{\boldsymbol{T}}\hat{\boldsymbol{y}}. \tag{7}$$

The optimal estimation kernel is chosen to minimize a cost function defined as

$$J_{nc} = \int_{-\infty}^{\infty} \mathbb{E}\left\{\boldsymbol{e}(t)^{\dagger}\boldsymbol{e}(t)\right\} dt, \tag{8}$$

where the estimation error is $\boldsymbol{e} = \tilde{\boldsymbol{z}} - \boldsymbol{z}$. By setting the derivative of the cost function to be zero, the optimal non-causal estimator is given as

$$\hat{\boldsymbol{T}}_{nc}(\omega) = \boldsymbol{R}_{zf}\hat{\boldsymbol{F}}\boldsymbol{R}_{yf}^{\dagger}\left(\boldsymbol{R}_{yf}\hat{\boldsymbol{F}}\boldsymbol{R}_{yf}^{\dagger} + \hat{\boldsymbol{N}}\right)^{-1}, \tag{9}$$

where $\hat{\boldsymbol{F}} = \mathbb{E}\left\{\hat{\boldsymbol{f}}\hat{\boldsymbol{f}}^{\dagger}\right\}$ and $\hat{\boldsymbol{N}} = \mathbb{E}\left\{\hat{\boldsymbol{n}}\hat{\boldsymbol{n}}^{\dagger}\right\}$ are the cross-spectral density matrix of nonlinear forcing and sensor noise, respectively. Furthermore, the optimal causal estimation kernel can be computed using the Wiener-Hopf formalism [29], which minimizes the cost function

$$J_c = \int_{-\infty}^{\infty} \mathbb{E}\left\{\boldsymbol{e}(t)^{\dagger}\boldsymbol{e}(t)\right\} + \left(\boldsymbol{\Lambda}_-(t)\boldsymbol{T}_c(t) + \boldsymbol{\Lambda}_-^{\dagger}(t)\boldsymbol{T}_c^{\dagger}(t)\right) dt, \tag{10}$$

where $\boldsymbol{\Lambda}_-$ is a Lagrange multiplier used to enforce causality of the estimation kernel, and the (+) and (−) subscripts indicates that the non-causal ($\tau < 0$) and causal ($\tau > 0$) portions of the functions are set to zero, respectively. By setting the derivative of Eq. (10) to be zero and solving the Wiener-Hopf problem, the causal estimation kernel is [29],

$$\hat{\boldsymbol{T}}_c(\omega) = \left(\boldsymbol{R}_{zf}\hat{\boldsymbol{F}}\boldsymbol{R}_{yf}^{\dagger}\left(\boldsymbol{R}_{yf}\hat{\boldsymbol{F}}\boldsymbol{R}_{yf}^{\dagger} + \hat{\boldsymbol{N}}\right)_-^{-1}\right)_+ \left(\boldsymbol{R}_{yf}\hat{\boldsymbol{F}}\boldsymbol{R}_{yf}^{\dagger} + \hat{\boldsymbol{N}}\right)_+^{-1}. \tag{11}$$

C. Resolvent-based control

The control framework is similar to the estimation framework. First, we define the control kernel for the noise-driven system in Eq. (2), which computes the actuation values based on the convolution of the kernel and the sensor signals [29],

$$\boldsymbol{a}(t) = \int_{-\infty}^{\infty} \boldsymbol{\Gamma}(t-\tau)\boldsymbol{y}_f(\tau)d\tau, \tag{12}$$

where $\boldsymbol{\Gamma} \in \mathbb{C}^{n_a \times n_y}$ is the control kernel. The non-causal control problem is solved by minimizing the cost function

$$J_{nc} = \int_{-\infty}^{\infty} \mathbb{E}\left\{\boldsymbol{z}(t)^{\dagger}\boldsymbol{z}(t) + \boldsymbol{a}(t)^{\dagger}\boldsymbol{P}\boldsymbol{a}(t)\right\} dt, \tag{13}$$

where $\boldsymbol{P} \in \mathbb{C}^{n_a \times n_a}$ is a positive-definite matrix that defines actuation penalties. By minimizing the cost function, the optimal non-causal control is obtained as

$$\hat{\boldsymbol{\Gamma}}_{nc}(\omega) = \left(\boldsymbol{R}_{za}^{\dagger}\boldsymbol{R}_{za} + \hat{\boldsymbol{P}}\right)^{-1}\left(-\boldsymbol{R}_{za}^{\dagger}\right)\boldsymbol{R}_{zf}\hat{\boldsymbol{F}}\boldsymbol{R}_{yf}^{\dagger}\left(\boldsymbol{R}_{yf}\hat{\boldsymbol{F}}\boldsymbol{R}_{yf}^{\dagger} + \hat{\boldsymbol{N}}\right)^{-1}. \tag{14}$$

The causal control problem is solved by introducing Lagrange multipliers. The cost function is defined as

$$J_c = \int_{-\infty}^{\infty} \mathbb{E}\left\{\boldsymbol{z}(t)^{\dagger}\boldsymbol{z}(t) + \boldsymbol{a}(t)^{\dagger}\boldsymbol{P}\boldsymbol{a}(t) + \left(\boldsymbol{\Lambda}_-(t)\boldsymbol{\Gamma}_c(t) + \boldsymbol{\Lambda}_-^{\dagger}(t)\boldsymbol{\Gamma}_c^{\dagger}(t)\right)\right\} dt. \tag{15}$$

Through minimizing the cost function and solving the Wiener-Hopf problem, the optimal causal control kernel is

$$\begin{aligned}\hat{\boldsymbol{\Gamma}}_c(\omega) = &\left(\boldsymbol{R}_{za}^{\dagger}\boldsymbol{R}_{za} + \hat{\boldsymbol{P}}\right)_+^{-1}\left(\left(\boldsymbol{R}_{za}^{\dagger}\boldsymbol{R}_{za} + \hat{\boldsymbol{P}}\right)_-^{-1}\left(-\boldsymbol{R}_{za}^{\dagger}\right)\boldsymbol{R}_{zf}\hat{\boldsymbol{F}}\boldsymbol{R}_{yf}^{\dagger}\right.\\ &\left.\left(\boldsymbol{R}_{yf}\hat{\boldsymbol{F}}\boldsymbol{R}_{yf}^{\dagger} + \hat{\boldsymbol{N}}\right)_-^{-1}\right)_+ \left(\boldsymbol{R}_{yf}\hat{\boldsymbol{F}}\boldsymbol{R}_{yf}^{\dagger} + \hat{\boldsymbol{N}}\right)_+^{-1}.\end{aligned} \tag{16}$$

Considering the full linear system in Eq. (1), the final closed-loop control kernel that is convolve with the full measurement $\boldsymbol{y}(t)$ is

$$\hat{\boldsymbol{\Gamma}}' = \left(\boldsymbol{I} + \hat{\boldsymbol{\Gamma}}\boldsymbol{R}_{ya}\right)^{-1}\hat{\boldsymbol{\Gamma}}, \tag{17}$$

where $\hat{\boldsymbol{\Gamma}}$ is the causal or non-causal control kernel derived from noise-driven system.

D. Implementation

The numerical method follows the previous work of Towne et al. [32]. The linear solver is implemented within the framework of CharLES. The details of the solver are introduced by Brès et al. [36]. We use the three-dimensional compressible Navier-Stokes equations for a perfect gas,

$$\frac{\partial}{\partial t}\begin{pmatrix}\rho\\ \rho u_i\\ \rho E\end{pmatrix} + \frac{\partial}{\partial x_j}\begin{pmatrix}\rho u_j\\ \rho u_i u_j + p\delta_{ij}\\ (\rho E + p)u_j\end{pmatrix} = \frac{\partial}{\partial x_j}\begin{pmatrix}0\\ \tau_{ij}\\ \tau_{kj}u_j - q_j\end{pmatrix}, \tag{18}$$

where ρE is the total energy, and the equation is closed using the ideal gas law $p = \rho RT$. Fourier's Law, $q_j = -\kappa\frac{\partial T}{\partial x_j}$, gives the heat flux q_j, and the Newtonian viscous stress tensor is

$$\tau_{ij} = \mu\left(\frac{\partial u_i}{\partial x_j} + \frac{\partial u_j}{\partial x_i} - \frac{2}{3}\frac{\partial u_k}{\partial x_k}\delta_{ij}\right). \tag{19}$$

Eq. (18) can be described in the operator form

$$\frac{\partial \boldsymbol{q}}{\partial t} = \mathcal{F}(\boldsymbol{q}), \tag{20}$$

where $\boldsymbol{q}$ is the state vector on the discretized mesh that contains all the degrees of freedom in the system, and $\mathcal{F}$ is nonlinear Navier-Stokes operator. We apply the Reynolds decomposition

$$\boldsymbol{q}(x,t) = \overline{\boldsymbol{q}}(x) + \boldsymbol{q}'(x,t). \tag{21}$$

Here, the perturbation is defined as

$$\boldsymbol{q}' = \begin{bmatrix} \rho' \\ (\rho u)' \\ (\rho v)' \\ (\rho w)' \\ (\rho E)' \end{bmatrix} = \begin{bmatrix} \rho' \\ \rho'\bar{u} + \bar{\rho}u' \\ \rho'\bar{v} + \bar{\rho}v' \\ \rho'\bar{w} + \bar{\rho}w' \\ \bar{\rho}(\bar{u}u' + \bar{v}v' + \bar{w}w') + \frac{1}{2}\rho'(\bar{u}^2 + \bar{v}^2 + \bar{w}^2) + \frac{p'}{\gamma - 1} \end{bmatrix}, \tag{22}$$

where the overbar notation denotes time-averaged values, and γ is the adiabatic index for the ideal gas. Applying the decomposition in Eq. (21), we get the linearized operator form

$$\frac{\partial \boldsymbol{q}'}{\partial t} = \boldsymbol{A}\boldsymbol{q}' + \boldsymbol{f}'. \tag{23}$$

Here, $\boldsymbol{A} = \frac{\partial \mathcal{F}}{\partial \boldsymbol{q}}(\overline{\boldsymbol{q}})$ is the linearized Navier-Stokes operator, and $\boldsymbol{f}'$ is the combination of the nonlinear dynamics and external forcing on the system. In this work, the linearized Navier-Stokes operator $\boldsymbol{A}$ is explicitly constructed using the matrix-forming approach. The linear operator is extracted from the CharLES ideal gas solver by perturbing each degree of freedom. To reduce computational expense, we adopt an approach similar to that of Nielsen and Kelb [37], in which many degrees of freedom are simultaneously perturbed using non-overlapping numerical stencils. All stencil data is gathered on a single processor, where the domain is sorted into lists of non-overlapping degrees of freedom. These lists are then broadcast to all other processors. We utilize the open-source PETSc library [38] to perform large-scale linear algebra computations associated with the linear operator $\boldsymbol{A}$.

Direct computation of estimation/control kernels requires evaluating the resolvent operators $\boldsymbol{R}$, which involves inverting a large matrix and typically scales poorly with system size (e.g., $O(n^2)$ for LU-based methods [39]). To address this, a time-stepping approach based on [27–29] is adopted to efficiently capture the time-dependent behavior of modified resolvent operators at a reduced computational cost of $O(n)$.

The modified resolvent operator $\boldsymbol{R_{za}}$ and $\boldsymbol{R_{ya}}$ in Eq. (16) and Eq. (14), respectively, can be computed by simulating a series of impulse responses of the actuation system Eq. (3),

$$\frac{d\boldsymbol{q}_{a,k}}{dt}(t) = \mathbf{A}\boldsymbol{q}_{a,k}(t) + \boldsymbol{B}_{a,k}\delta(t), \tag{24a}$$

$$\boldsymbol{y}_{a,k}(t) = \boldsymbol{C}_y\boldsymbol{q}_{a,k}(t), \tag{24b}$$

$$\boldsymbol{z}_{a,k}(t) = \boldsymbol{C}_z\boldsymbol{q}_{a,k}(t), \tag{24c}$$

where, $\boldsymbol{y}_{a,k} \in \mathbb{C}^{n_y}$ and $\boldsymbol{z}_{a,k} \in \mathbb{C}^{n_z}$ are sensor and target measurements of the direct system forced by the impulse $\delta(t)$ located at k-th actuator, which is the k-th column of the actuation matrix $\boldsymbol{B}_{a,k}$. By collecting these data for each actuator and taking the Fourier transform, we obtain

$$\boldsymbol{R}_{ya} = \begin{bmatrix} \hat{\boldsymbol{y}}_{a,1} & \hat{\boldsymbol{y}}_{a,2} & \cdots & \hat{\boldsymbol{y}}_{a,n_a} \end{bmatrix}, \tag{25a}$$

$$\boldsymbol{R}_{za} = \begin{bmatrix} \hat{\boldsymbol{z}}_{a,1} & \hat{\boldsymbol{z}}_{a,2} & \cdots & \hat{\boldsymbol{z}}_{a,n_a} \end{bmatrix}. \tag{25b}$$

The combination of two modified resolvent operators $\boldsymbol{R}_{yf}\boldsymbol{R}_{yf}^{\dagger}$ and $\boldsymbol{R}_{zf}\boldsymbol{R}_{yf}^{\dagger}$, used in both the estimation and control kernels, can be computed more efficiently through the combination of an adjoint run and a linear run. First, the time marching of an adjoint system is performed for the sensor i,

$$\begin{aligned} -\frac{d\boldsymbol{q}_{f,i}}{dt}(t) &= \boldsymbol{A}^{\dagger}\boldsymbol{q}_{f,i}(t) + \boldsymbol{C}_{y,i}^{\dagger}\delta(t), \\ s_i(t) &= \boldsymbol{B}_f^{\dagger}\boldsymbol{q}_{f,i}(t), \end{aligned} \tag{26}$$

where $\boldsymbol{A}^\dagger$ is the adjoint system matrix, $\boldsymbol{C}^\dagger_{y,i}$ is the adjoint sensor matrix, and $\boldsymbol{B}^\dagger_f$ is the adjoint matrix that selects the spatial support of the forcing. The measurement $s_i(t)$ is collected and stored for each time step. Then, another linear run is performed in which $s_i(t)$ is used as a forcing,

$$\begin{aligned} \frac{d\boldsymbol{q}_{f,i}}{dt}(t) &= \boldsymbol{A}\boldsymbol{q}_{f,i}(t) + \boldsymbol{B}_f s_i(t), \\ \boldsymbol{y}_{f,i}(t) &= \boldsymbol{C}_y \boldsymbol{q}_{f,i}(t) + \boldsymbol{n}_i(t), \\ z_{f,i}(t) &= \boldsymbol{C}_z \boldsymbol{q}_{f,i}(t). \end{aligned} \tag{27}$$

The Fourier transformation of the adjoint-linear run result $z_{f,i}\ \boldsymbol{y}_{f,i}$ yields the modified resolvent operator products

$$\begin{aligned} \boldsymbol{R}_{yf}\boldsymbol{R}^\dagger_{yf} &= \left[\begin{array}{cccc} \hat{\boldsymbol{y}}_1 & \hat{\boldsymbol{y}}_2 & \dots & \hat{\boldsymbol{y}}_{n_y} \end{array}\right], \\ \boldsymbol{R}_{zf}\boldsymbol{R}^\dagger_{yf} &= \left[\begin{array}{cccc} \hat{\boldsymbol{z}}_1 & \hat{\boldsymbol{z}}_2 & \dots & \hat{\boldsymbol{z}}_{n_y} \end{array}\right]. \end{aligned} \tag{28}$$

Martini et al. [29] show that the modified resolvent operator products can also be approximated using experimental or simulation data, which follows

$$\begin{bmatrix} \boldsymbol{S}_{y,y} & \boldsymbol{S}_{y,z} \\ \boldsymbol{S}_{z,y} & \boldsymbol{S}_{z,z} \end{bmatrix} = \begin{bmatrix} \boldsymbol{R}_{yf} \\ \boldsymbol{R}_{zf} \end{bmatrix} \hat{\boldsymbol{F}} \begin{bmatrix} \boldsymbol{R}^\dagger_{yf} & \boldsymbol{R}^\dagger_{zf} \end{bmatrix} + \begin{bmatrix} \hat{\boldsymbol{N}} & 0 \\ 0 & 0 \end{bmatrix}, \tag{29}$$

where $\boldsymbol{S}_{y,z}$ and $\boldsymbol{S}_{z,y}$ are cross spectral density matrices and $\boldsymbol{S}_{y,y}$ and $\boldsymbol{S}_{z,z}$ are power spectral density matrices. As a result, from Eq. (8), Eq. (11), Eq. (14), and Eq. (16), the control and estimation kernel can be computed in a data-driven manner.

III. Supersonic jet results

A. Simulation setup

To obtain data that will be used for numerous purposes – forming data-driven estimation kernels, extracting sensor measurements and ground-truth target measurements, exploring sensor and target placement, and providing physical insight for interpreting results – we perform a large-eddy simulation (LES) of a supersonic jet using the CharLES solver. Following the configuration presented by Brès et al. [36], the jet has a Mach number of $M_j = 1.5$ and is isothermal ($T_j/T_\infty = 1$). The nozzle pressure ratio is set to 3.67 and the nozzle temperature ratio to 1.45, producing a jet that approximates an ideally expanded condition. The three-dimensional unstructured mesh contains 33 million control volumes. The simulation spans 3000 acoustic time units with a time step of 0.0002. A full flow-field snapshot is recorded every 100 time steps, resulting in a total of 150,000 snapshots. The simulation was performed on the Department of Defense's Onyx supercomputing platform and consumes a total of 3 million core-hours. Figure 1 shows a snapshot of the isothermal, ideally expanded jet and its streamwise mean velocity profile. Despite systemetic tuning of the nozzle pressure ratio and other parameters, weak shocks remain present near the nozzle lip, indicating a small but non-negligible deviation from ideal expansion.

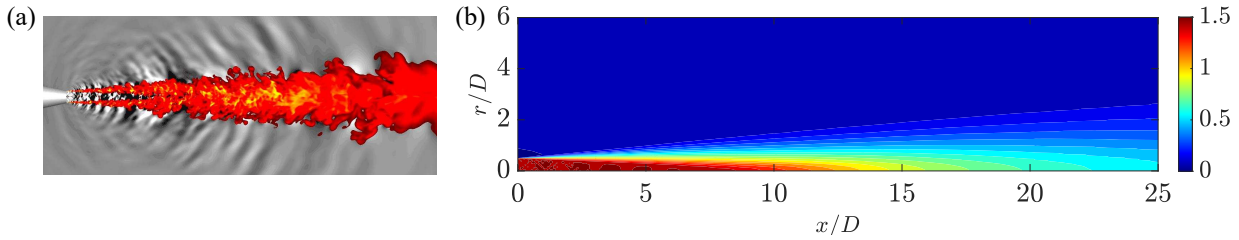

Fig. 1 Visualization of the Mach 1.5 isothermal jet: (a) one instantaneous snapshot of the temperature and pressure fields; (b) mean streamwise velocity.

B. Data-driven estimation

One of the primary objectives of this study is to optimize the sensor configuration for supersonic jet wavepacket estimation. To this end, we employ data-driven methods informed by large eddy simulation (LES) results, which provide valuable insight into wavepacket dynamics and allow systematic evaluation of sensor placement strategies.

Sensor and target measurements are extracted from the LES snapshots using a Gaussian spatial support of the form

$$\alpha \exp\left[-\frac{(x-x_c)^2}{2\sigma_x^2} - \frac{(r-r_c)^2}{2\sigma_r^2}\right], \tag{30}$$

where σ_x and σ_r are standard deviations that determine the width of the Gaussian function, x_c and r_c specify the location of the sensor or target, and α normalizes the integral of the function. We use $\sigma_x = \sigma_r = 0.05$ for all sensors and targets.

An azimuthal Fourier transform is performed to extract the first 10 azimuthal modes from the spatially weighted LES data. Subsequently, a blockwise Fourier transform is applied in the time domain using a Hanning window, enabling computation of the cross-spectral density and power spectral density matrices in Eq. (29). The non-causal estimation kernel is then constructed using Eqs. (9) and (29), and estimation is performed over the time interval $\frac{tc}{D} \in [180, 200]$.

To quantify estimation accuracy, we define the error metric as

$$\epsilon = \frac{\sum_i \int (\tilde{z}_i(t) - z_i(t))^2 \, dt}{\sum_i \int (z_i(t))^2 \, dt}, \tag{31}$$

where $\tilde{z}_i$ and z_i denote the estimated and actual(LES) values for target i, respectively.

First, we consider single-sensor, single-target estimation and present results for two distinct configurations. The first configuration focuses on a near-nozzle lipline wavepacket, with sensor and target positions given by $(x/D, r/D)_y = (0.6, 0.5)$ and $(x/D, r/D)_z = (2, 0.5)$, respectively. Here, $(\cdot,\cdot)_y$ and $(\cdot,\cdot)_z$ indicate sensor and target positions, respectively. The second configuration examines a downstream centerline perturbation, specifically $(x/D, r/D)_y = (5, 0)$ and $(x/D, r/D)_z = (6, 0)$. Figure 2 presents the estimation results for both configurations, alongside the LES target values. Figure 2(c) demonstrates that the estimation error becomes substantial when utilizing a sensor located near the nozzle, highlighting the difficulty of accurately capturing downstream wavepackets in this region. Conversely, Figure 2(d) reveals comparatively accurate estimation for downstream sensors and targets. These results suggest the existence of coherent structures within the potential core when measurements are acquired sufficiently far from the near-nozzle region.

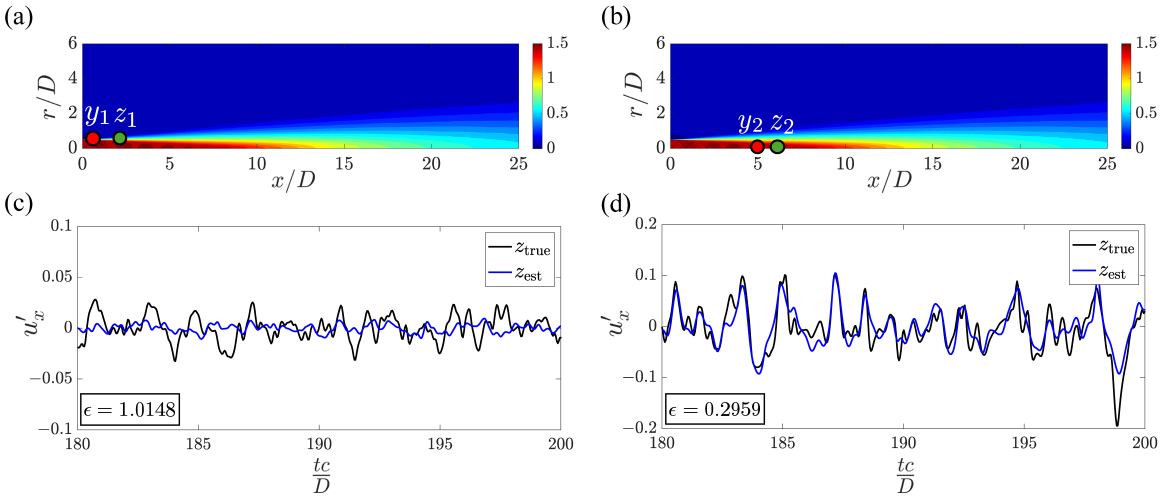

Fig. 2 Single sensor data-driven estimation results compared with LES. (1.a) Estimation kernel for configuration 1: sensor at $y = (0.6, 0.5)$, target at $z = (2, 0.5)$. (1.b) Estimation result for configuration 1 (blue line), compared with LES target value (black line). (2.a) Estimation kernel for configuration 2: sensor at $y = (5, 0)$, target at $z = (6, 0)$. (2.b) Estimation result for configuration 2 (blue line), compared with LES target value (black line).

To assess whether multiple near-field sensors enhance estimation accuracy, we employ both axial and radial sensor arrays. The axial array is positioned along the lipline at $r/D = 0.5$, extending from $x/D = 0.2$ to $x/D = 0.6$ with a spacing of $\Delta x/D = 0.1$. The radial array is located at $x/D = 0.6$, spanning $r/D = 0.1$ to $r/D = 0.5$ with a spacing of $\Delta r/D = 0.1$. Data-driven estimation is then performed using all sensors from each configuration to estimate a series of target locations along both the jet centerline ($r/D = 0$) and the lipline ($r/D = 0.5$), both within $x/D \in [1.0, 10.8]$. The estimation results are compared to those obtained using a single sensor positioned at $(x/D, r/D) = (0.6, 0.5)$. Figure 3(a) illustrates the multi-sensor and target configurations.

For lipline targets, as shown in Figure 3(b), the estimation error associated with the single near-nozzle sensor is initially low but increases rapidly as the target location moves downstream, eventually saturating near $x/D = 2$. Employing either the radial or axial sensor array provides moderate improvements in estimation accuracy within the near-nozzle region, with the radial array yielding slightly better performance.

For centerline targets, both sensor arrays outperform the single-sensor configuration for $x/D < 1.2$; however, estimation errors subsequently increase, with the radial array exhibiting a comparatively slower rate of error growth than both the axial array and the single-sensor case. This improved performance may be attributed to the radial array's greater number of sensors positioned closer to the nozzle centerline. These results suggest that deploying additional sensors within the region $r/D < 0.5$ may be necessary to more effectively capture centerline fluctuations.

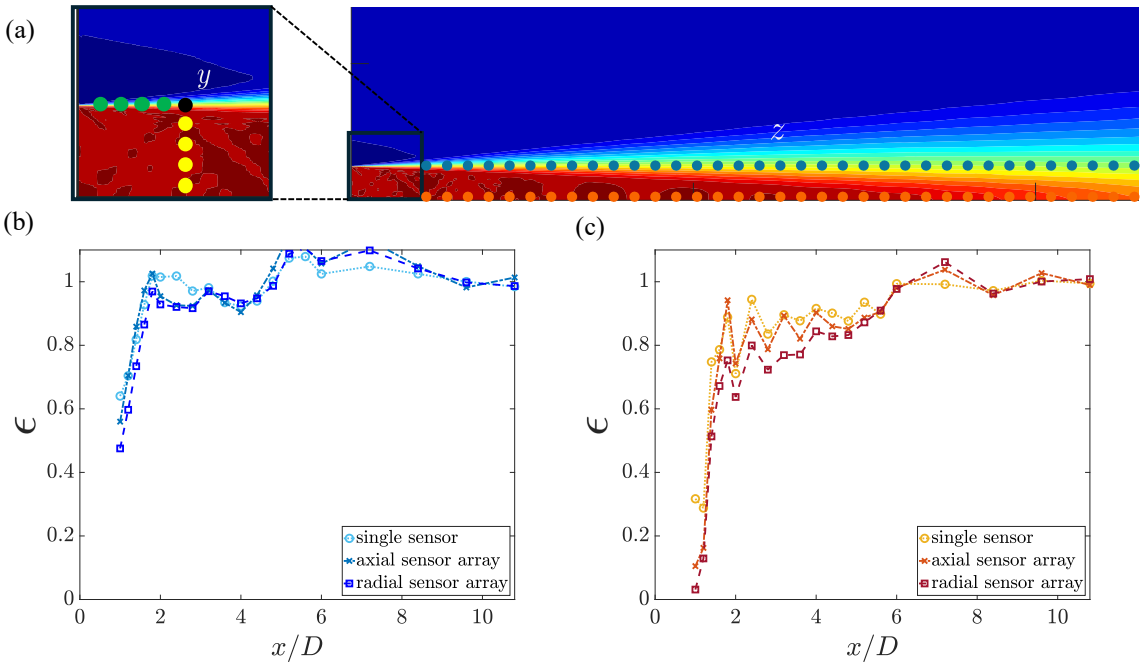

Fig. 3 Multi-sensor data-driven estimation results for the supersonic jet: (a) sensor layout: single near lip sensor (black dot), axial sensor array (green + black dots), radial sensor array (yellow + black dots); (b) Estimation error for lip line targets (blue dots); (c) Estimation error for centerline targets (orange dots).

To better explain the single sensor single target behavior, for several sensor locations, we plot their coherence with the rest of the flow field. The sensor-target coherence is defined as

$$\gamma_{yz} = \frac{|S_{yz}|}{\sqrt{S_{yy}}\sqrt{S_{zz}}}. \tag{32}$$

The coherence results shown in figure 4 give us a better understanding of the previous estimation results. Fig. 4(a) indicates that even weak shocks interact with the flow and confine high coherence to the near field, as evidenced by coherence contours that closely follow the shape of oblique and reflected shocks. This helps explain why a single sensor located near the nozzle yields poor estimation results. Furthermore, since the region of high coherence extends slightly farther downstream along the centerline than along the lipline, it explains why lipline targets suffer more from

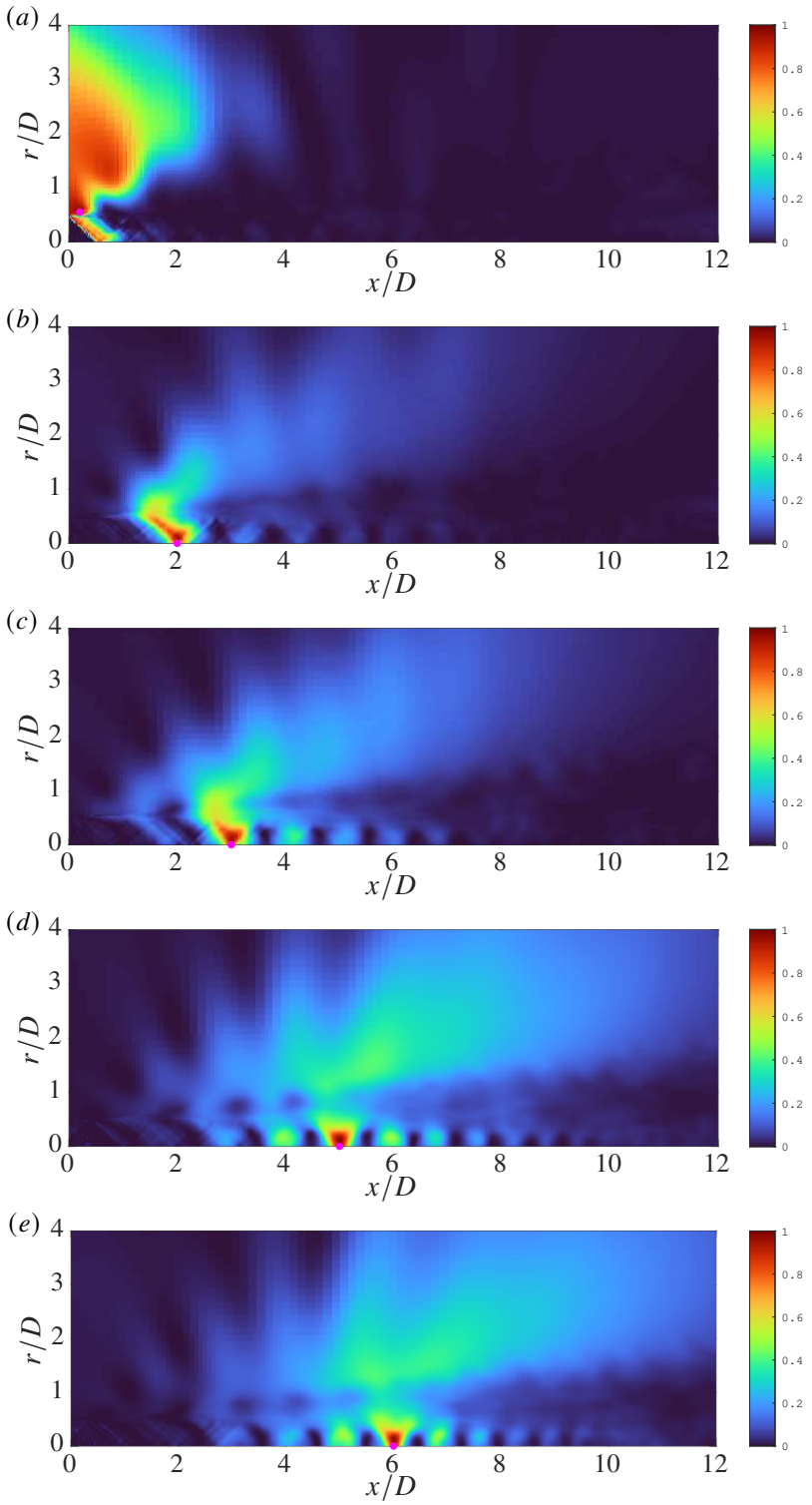

Fig. 4 Streamwise velocity coherence γ_{yz} at $St = 0.3$ for: (a) $y = (0.2, 0.55)$, (b) $y = (2, 0)$, (c) $y = (3, 0)$, (d) $y = (5, 0)$, (e) $y = (6, 0)$.

using a single upstream sensor and why a relatively larger benefit can be achieved by placing sensors slightly farther downstream or by increasing the number of sensors in that region (as seen in figure 3(c)).

Figure 4(b) and (c) further illustrate that, in the near field, shock structures confine regions of high coherence within individual shock cells. However, figure 4(d) and (e) show that, as the flow moves downstream and the shock cells weaken, coherent structures begin to extend across multiple cells, resulting in improved spatial coherence. This observation aligns with figure 2(b), where both the sensor and target are located within these high-coherence regions, leading to more accurate estimation results. These findings highlight the necessity of enhancing near-nozzle to far-field coherence, such as by weakening the near-nozzle shock structures, in order to more effectively utilize near-field sensors for downstream wavepacket estimation and control.

C. Linear system set up

As the first step toward the overarching goal of controlling the three-dimensional nonlinear jet, we perform estimation and control on fluctuations corresponding to the leading azimuthal mode ($m = 0$) of the linearized jet using a two-dimensional, asymmetric model. The two-dimensional mesh comprising approximately 0.4 million cells is generated using Pointwise. The linear system is subjected to external forcing in the nozzle's diverging region; specifically, a random external perturbation modeled as white noise is applied to control volumes within the region $x/D \in [-0.7,\ -0.1]$ and $r/D \in [0,\ 0.5]$. The linear system is simulated for a total of 300 acoustic time units with a time step of $dt = 0.0002$. Figure 5 presents an instantaneous snapshots of the streamwise momentum fluctuations in the linear system. The wavepacket structures generated in the linear system can be observed along the nozzle lip.

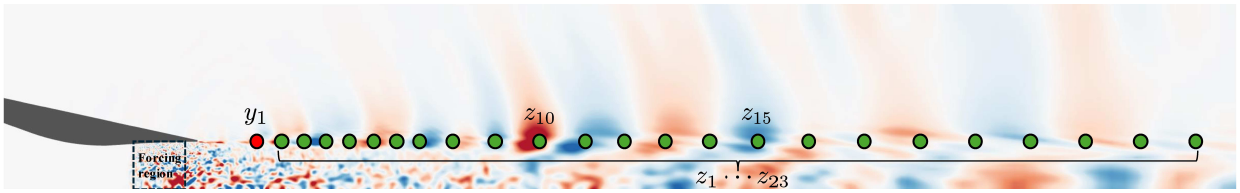

Fig. 5 Instantaneous snapshot of the streamwise momentum fluctuation, $\rho u_x'$. The external forcing region (black box) spans $x/D \in [-0.7, -0.1]$ and $r/D \in [0, 0.5]$. Sensor and target locations for operator-based estimation are shown: the near-nozzle sensor y_1 (red dot) is located at $x/D = 0.6$, $r/D = 0.5$, and an array of targets z_1 through z_{23} is distributed along $x/D \in [1.0, 10.8]$ at a fixed radius $r/D = 0.5$. The targets z_{10} ($x/D = 2.0$, $r/D = 0.5$) and z_{15} ($x/D = 5.2$, $r/D = 0.5$) are picked to show estimated values compared with LES data.

D. Resolvent-based estimation for the linear system

We present resolvent-based estimation results and compare them with the true streamwise momentum fluctuation, $\rho u_x'$. Based on the approach described in Sections II.B and II.D, adjoint-linear simulations are performed to construct the estimation kernels. The spatial support for both the sensor and target is identical to that used in the data-driven estimation. Furthermore, the temporal support for actuation in the adjoint-linear simulations is defined by a Gaussian distribution with $\sigma_t = 12.5$. Sensor noise is modeled as white noise, with a cross-spectral density (CSD) given by $\hat{\boldsymbol{N}} = \varepsilon I$, where ε is set to 1% of the maximum value of $\hat{\boldsymbol{Y}}$.

First, we present the estimation results for two downstream targets within the lipline target array, utilizing a single sensor positioned near the nozzle. Specifically, sensor y_1 is located at $x/D = 0.6$ and $r/D = 0.5$, as illustrated in Figure 5. The first target, z_{10}, is located at $x/D = 2.0$ and $r/D = 0.5$, while the second target, z_{15}, is positioned at $x/D = 5.2$ and $r/D = 0.5$. For both cases, we measure and estimate the streamwise momentum fluctuation, $\rho u_x'$. The corresponding estimation kernels and results are shown in Figure 6.

A comparison of the estimation kernel plots in Figure 6(a) and Figure 6(b) reveals two physically consistent trends. First, the estimation kernel for z_{15} is shifted to the right along the time axis relative to that of z_{10}, indicating that perturbations require more time to reach targets located further downstream. Second, the magnitude of the estimation kernel for z_{15} is smaller than that for z_{10}, consistent with the decrease in RMS values along the downstream lipline observed in both experiments and simulations. Importantly, both estimation kernels are nearly causal. As shown in Figure 6(c) and Figure 6(d), estimation errors for both targets are less than 3%, with the second target demonstrating slightly higher accuracy.

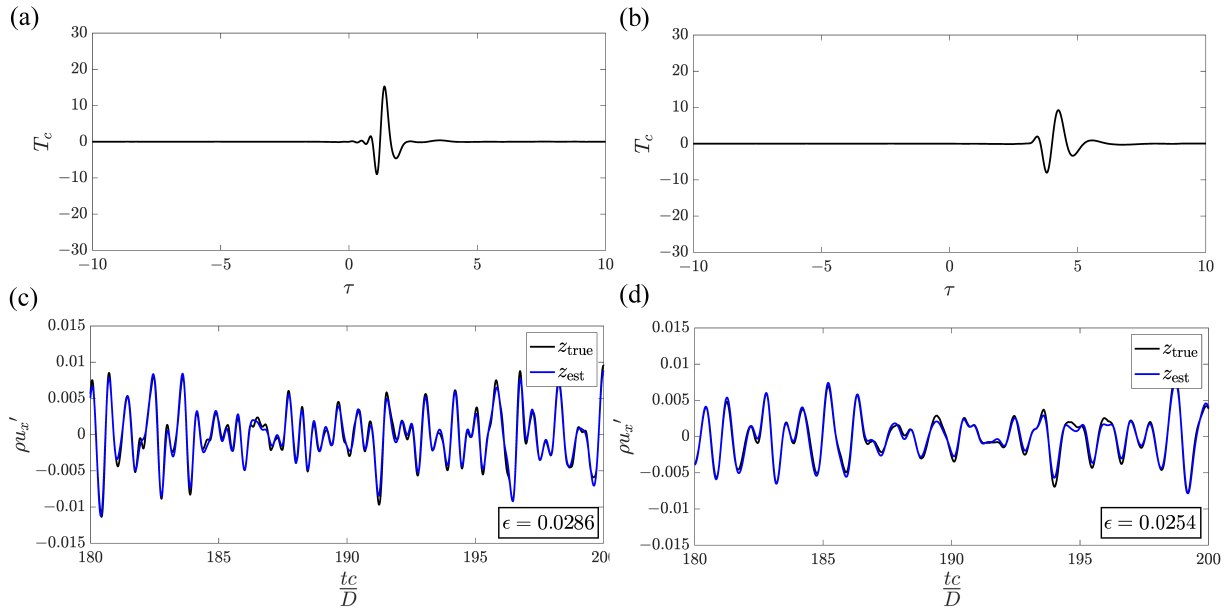

Fig. 6 Operator-based estimation results for single targets. (a) Estimation kernel for z_{10}. (b) Estimation kernel for z_{15}. (c) Estimation result for z_{10} (blue line), compared with the true target value (black line). (d) Estimation result for z_{15} (blue line), compared with the true target value (black line).

To further characterize estimation errors across a range of target positions in the downstream region, we estimate the signal at all targets within the array along the lipline, spanning $x/D \in [1.0,\ 10.8]$ at a fixed radius $r/D = 0.5$. This configuration is consistent with the lipline arrangement used in Section III.B. The sensor and target layout are depicted in Figure 5.

For multiple-target estimation, the same adjoint-linear procedure used in single-target estimation is employed to construct the estimation kernel, with the distinction that an extended target matrix C_z is utilized. The resulting estimation errors for the target array are presented in Figure 7. We found that the estimation error can reach up to 10% at $x/D = 1$, but gradually decreases for targets located further downstream. This trend may result from the external disturbance being applied directly at the nozzle's diverging region, placing it very close to $x/D = 1$. Consequently, when the target is not sufficiently close to the sensor but is in proximity to the external disturbance, the estimation error increases. As targets move downstream, the estimation error decreases rapidly, achieving a minimum of $\epsilon = 0.0218$ near $x/D = 3$. As the target location extends further away from the estimator, the error gradually increases; however, the overall estimation error remains below 7% up to $x/D = 10$. These findings suggest that our resolvent-based framework is capable of accurately estimating downstream wavepackets, provided that the nonlinear forcing is appropriately modeled.

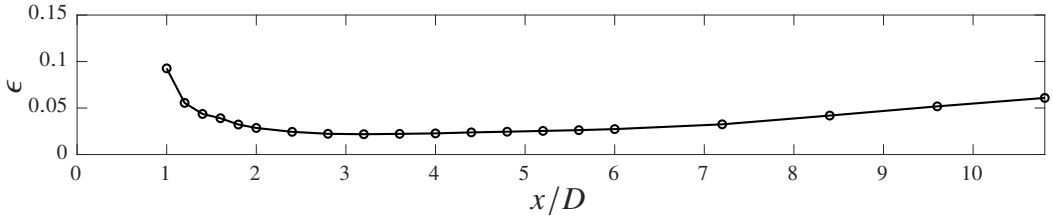

Fig. 7 Estimation error for the target array along the nozzle lip-line for the linearized jet.

E. Resolvent-based control for the linear system

Motivated by the resolvent-based estimation results, we selected a target along the lipline and placed the actuator downstream of $x/D = 1$ to maximize control effectiveness. As illustrated in Figure 8, the sensor is located at $x/D = 0.6$, $r/D = 0.5$, the actuator at $x/D = 3.0$, $r/D = 0.5$, and the target at $x/D = 5.2$, $r/D = 0.5$. The spatial support for each sensor, actuator, and target follows the same Gaussian function utilized in the estimation procedure.

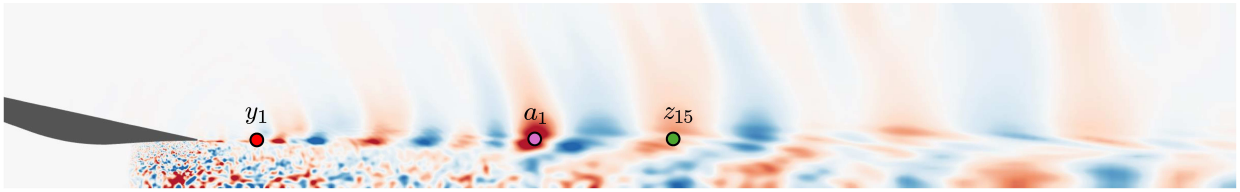

Fig. 8 Layout of the sensor y_1 (red dot at $x/D = 0.6$), actuator a_1 (mauve dot at $x/D = 3.0$), and target z_{15} (green dot at $x/D = 5.2$), all positioned along the lipline at $r/D = 0.5$, for closed-loop control of the linear jet.

The linear-adjoint run result from the resolvent-based estimation is reused, along with an additional actuated linear run, to construct the control kernel, which is shown in Figure 9. Since the optimal controller is non-causal and exhibits relatively large fluctuations for $\tau < 0$, a Wiener–Hopf decomposition is performed to enforce causality and improve the control performance.

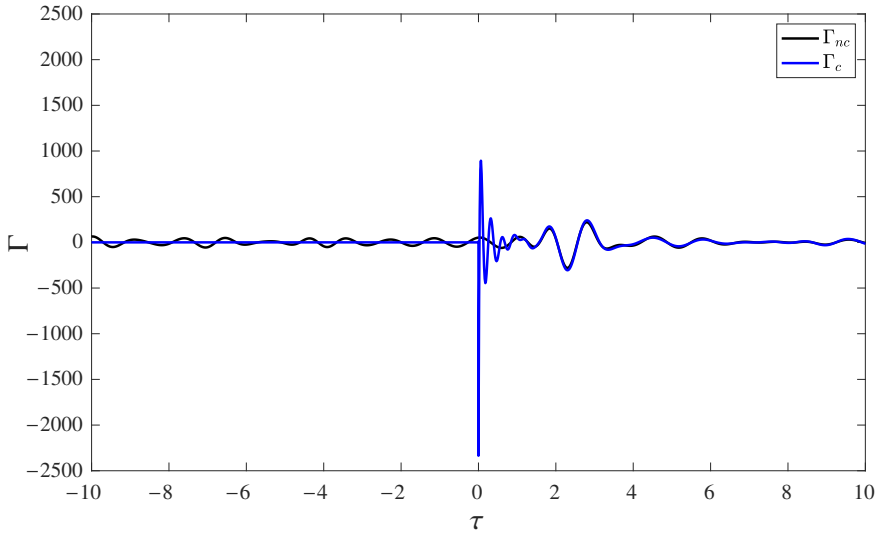

Fig. 9 Control kernels: non-causal kernel (black line), causal kernel (blue line).

After computing the causal control kernel, we simulate the controlled case, with the sensor activated for $\frac{tc}{D} > 80$, over a duration of 270 acoustic time units. Figure 10 compares the controlled and uncontrolled cases. The results demonstrate that the controller attenuates a portion of the prominent peaks in the uncontrolled signal.

To better quantify the effectiveness of the controller, we compute the root mean square (RMS), defined as

$$\mathrm{RMS}_{\mathrm{discrete}} = \sqrt{\frac{1}{T}\sum_{i=1}^{N} z_i^2\,\Delta t}, \tag{33}$$

where z_i denotes the variable of interest, N is the number of discrete time points, Δt is the time step, and T is the total duration.

The RMS values of the streamwise momentum fluctuation, $(\rho u_x{}')_{\mathrm{RMS}}$, are 0.37 for the uncontrolled case and 0.24 for the controlled case. This corresponds to a 34% reduction in RMS due to control, which suggests a partial mitigation of the underlying wavepacket structure.

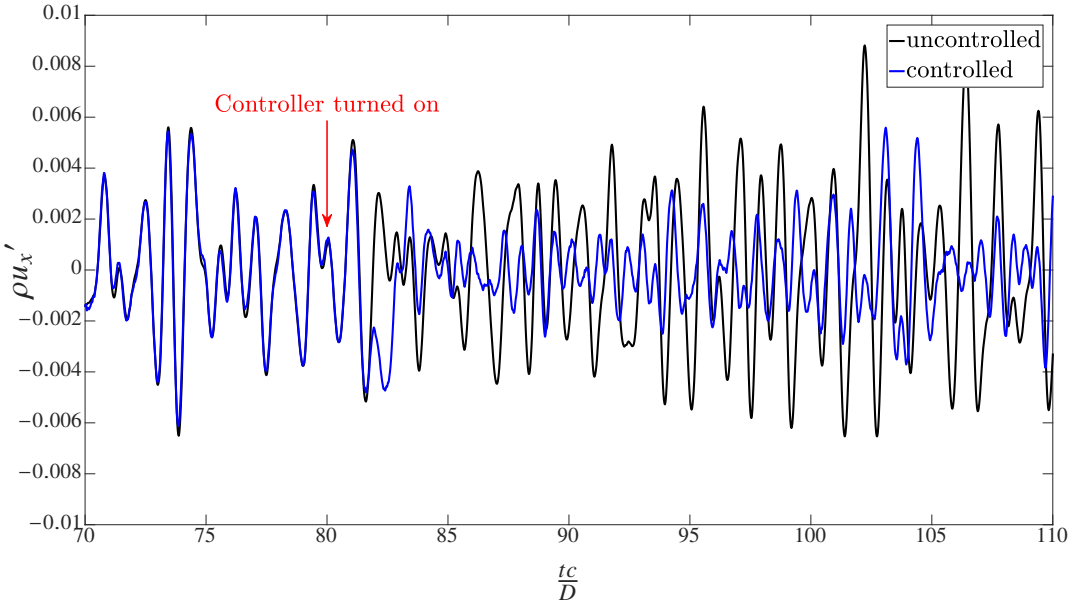

Fig. 10 Comparison between the uncontrolled target value (black line) and the controlled target value (blue line).

IV. Conclusions and future work

This paper presents further progress toward the goal of using resolvent-based methods to reduce turbulent mixing noise in supersonic jets.

First, we performed data-driven estimation using LES data for a Mach 1.5 turbulent jet. The results indicate that strong nonlinearity exists in the near-nozzle region, accompanied by significant shock-turbulence interaction, which reduces estimation accuracy for sensors and targets located near the nozzle. However, further downstream at the rear of the potential core, coherent structures are better defined, leading to improved estimation performance. Additionally, we demonstrate that employing multiple sensors can moderately improve estimation accuracy in the near-nozzle region.

Second, we demonstrated the feasibility of resolvent-based estimation for the linearized jet. The estimated target values closely match those obtained from direct linear simulations, validating the proposed framework. Minor discrepancies appear in the region near the nozzle, which might be due to the forcing region being placed too close to the targets, but our resolvent framework is able to maintain high estimation accuracy with $\epsilon < 7\%$ up to $x/D = 10.8$, using a single near-nozzle lip-line sensor at $x/D = 0.6$.

Third, we applied the resolvent-based control strategy to the linearized jet. Following the methodology proposed by Jung et al. [30], a Wiener–Hopf decomposition is used to derive a causal control kernel. We show that our framework is able to suppress downstream target fluctuations, reducing 34% of the root mean square of the streamwise momentum fluctuation $(\rho u_x')_{\mathrm{RMS}}$, using only one sensor and a single actuator.

A comparison of data-driven and resolvent-based estimation results indicates that developing more effective methods to address nonlinearity is essential for further improving estimator performance. Because estimation accuracy determines the upper bound of closed-loop control effectiveness, advancing these modeling strategies will be a central focus of our future research. Comparing the resolvent-based estimation and control results, we find that while the estimation method accurately predicts downstream wavepacket structures, a single actuator is insufficient for generating the fully inverted wavepackets. Future work will investigate strategies such as relocating actuators upstream, employing multiple actuators, or utilizing iterative control [30] to achieve greater fluctuation cancellation at the target location.

Acknowledgments

The U-M authors were funded in part by ONR grant no. N00014-22-1-2561.

References

[1] Saiyed, N., Bridges, J., and Mikkelsen, K., "Acoustics and thrust of separate-flow exhaust nozzles with mixing devices for high-bypass-ratio engines," *6th Aeroacoustics Conference and Exhibit*, 2000, p. 1961.

[2] Janardan, B., Hoff, G., Barter, J., Martens, S., Gliebe, P., Mengle, V., Dalton, W., and Saiyed, N., "AST critical propulsion and noise reduction technologies for future commercial subsonic engines: separate-flow exhaust system noise reduction concept evaluation," Tech. rep., NASA, 2000.

[3] Lighthill, M. J., "On sound generated aerodynamically I. General theory," *Proceedings of the Royal Society of London. Series A. Mathematical and Physical Sciences*, Vol. 211, No. 1107, 1952, pp. 564–587.

[4] Martens, S., "Jet noise reduction technology development at GE aircraft engines," *ICAS paper*, Vol. 842, No. 2007-214495, 2002, p. 1.

[5] Peters, J. L., Zevitas, C. D., Redline, S., Hastings, A., Sizov, N., Hart, J. E., Levy, J. I., Roof, C. J., and Wellenius, G. A., "Aviation noise and cardiovascular health in the United States: a review of the evidence and recommendations for research direction," *Current Epidemiology Reports*, Vol. 5, 2018, pp. 140–152.

[6] Basner, M., Babisch, W., Davis, A., Brink, M., Clark, C., Janssen, S., and Stansfeld, S., "Auditory and non-auditory effects of noise on health," *The Lancet*, Vol. 383, No. 9925, 2014, pp. 1325–1332.

[7] Committee, N. R. A., et al., "Report on jet engine noise reduction," *URL: http://www. nrac. navy. mil/docs/2009_FINAL_Jet_Noise_Report_4-26-09. pdf*, 2009.

[8] Bridges, J., and Brown, C., "Parametric testing of chevrons on single flow hot jets," *10th AIAA/CEAS Aeroacoustics Conference*, 2004, p. 2824.

[9] Nesbitt, E., Brusniak, L., Underbrink, J., Lynch, D., and Martinez, M., "Effects of chevrons on engine jet noise structure," *13th AIAA/CEAS Aeroacoustics Conference (28th AIAA Aeroacoustics Conference)*, 2007, p. 3597.

[10] Rask, O., Kastner, J., and Gutmark, E., "Understanding how chevrons modify noise in supersonic jet with flight effects," *AIAA Journal*, Vol. 49, No. 8, 2011, pp. 1569–1576.

[11] Seiner, J., Ukeiley, L., and Jansen, B., "Aero-performance efficient noise reduction for the F404-400 engine," *11th AIAA/CEAS Aeroacoustics Conference*, 2005, p. 3048.

[12] Seiner, J., Jansen, B., and Murray, N., "Aero-performance efficient noise suppression of a supersonic model twin jet nacelle," *15th AIAA/CEAS Aeroacoustics Conference (30th AIAA Aeroacoustics Conference)*, 2009, p. 3130.

[13] Powers, R., and McLaughlin, D., "Acoustics measurements of scale models of military style supersonic beveled nozzle jets with interior corrugations," *18th AIAA/CEAS Aeroacoustics Conference (33rd AIAA Aeroacoustics Conference)*, 2012, p. 2116.

[14] Alapati, J. K., and Srinivasan, K., "Screech receptivity control using exit lip surface roughness for under-expanded jet noise reduction," *Physics of Fluids*, Vol. 36, No. 1, 2024.

[15] Krothapalli, A., Venkatakrishnan, L., Lourenco, L., Greska, B., and Elavarasan, R., "Turbulence and noise suppression of a high-speed jet by water injection," *Journal of Fluid Mechanics*, Vol. 491, 2003, pp. 131–159.

[16] Greska, B., and Krothapalli, A., "The near-field effects of microjet injection," *11th AIAA/CEAS Aeroacoustics Conference*, 2005, p. 3046.

[17] Castelain, T., Sunyach, M., Juvé, D., and Bera, J.-C., "Jet-noise reduction by impinging microjets: an acoustic investigation testing microjet parameters," *AIAA Journal*, Vol. 46, No. 5, 2008, pp. 1081–1087.

[18] Zaman, K., "Jet noise reduction by microjets: A parametric study," *15th AIAA/CEAS Aeroacoustics Conference (30th AIAA Aeroacoustics Conference)*, 2010, p. 3129.

[19] Samimy, M., Kim, J.-H., Kastner, J., Adamovich, I., and Utkin, Y., "Active control of a Mach 0.9 jet for noise mitigation using plasma actuators," *AIAA Journal*, Vol. 45, No. 4, 2007, pp. 890–901.

[20] Samimy, M., Kim, J.-H., and Kearney-Fischer, M., "Active control of noise in supersonic jets using plasma actuators," *Turbo Expo: Power for Land, Sea, and Air*, Vol. 48821, 2009, pp. 97–107.

[21] Samimy, M., Kearney-Fischer, M., Kim, J.-H., and Sinha, A., "High-speed and high-Reynolds-number jet control using localized arc filament plasma actuators," *Journal of Propulsion and Power*, Vol. 28, No. 2, 2012, pp. 269–280.

[22] Prasad, A. L. N., and Unnikrishnan, S., "Effect of plasma actuator-based control on flow-field and acoustics of supersonic rectangular jets," *Journal of Fluid Mechanics*, Vol. 964, 2023, p. A11.

[23] Prasad, A. L. N., and Unnikrishnan, S., "Noise mitigation in rectangular jets through plasma actuator-based shear layer control," *Journal of Fluid Mechanics*, Vol. 979, 2024, p. A16.

[24] Schmidt, O. T., Towne, A., Rigas, G., Colonius, T., and Bres, G. A., "Spectral analysis of jet turbulence," *Journal of Fluid Mechanics*, Vol. 855, 2018, pp. 953–982.

[25] Towne, A., Schmidt, O. T., and Colonius, T., "Spectral proper orthogonal decomposition and its relationship to dynamic mode decomposition and resolvent analysis," *Journal of Fluid Mechanics*, Vol. 847, 2018, pp. 821–867.

[26] Towne, A., Lozano-Durán, A., and Yang, X., "Resolvent-based estimation of space–time flow statistics," *Journal of Fluid Mechanics*, Vol. 883, 2020, p. A17.

[27] Martini, E., Cavalieri, A. V., Jordan, P., Towne, A., and Lesshafft, L., "Resolvent-based optimal estimation of transitional and turbulent flows," *Journal of Fluid Mechanics*, Vol. 900, 2020, p. A2.

[28] Martini, E., Rodríguez, D., Towne, A., and Cavalieri, A. V., "Efficient computation of global resolvent modes," *Journal of Fluid Mechanics*, Vol. 919, 2021, p. A3.

[29] Martini, E., Jung, J., Cavalieri, A. V., Jordan, P., and Towne, A., "Resolvent-based tools for optimal estimation and control via the Wiener–Hopf formalism," *Journal of Fluid Mechanics*, Vol. 937, 2022, p. A19.

[30] Jung, J., Bhagwat, R., and Towne, A., "Resolvent-based estimation and control of a laminar airfoil wake," *Journal of Fluid Mechanics*, Vol. 1016, 2025, p. A41.

[31] Jung, J., and Towne, A., "Resolvent-based estimation of a turbulent wake," *arXiv preprint arXiv:2507.18837*, 2025.

[32] Towne, A., Bhagwat, R., Zhou, Y., Jung, J., Martini, E., Jordan, P., Audiffred, D., Maia, I., and Cavalieri, A., "Resolvent-based estimation of wavepackets in turbulent jets," *30th AIAA/CEAS Aeroacoustics Conference (2024)*, 2024, p. 3413.

[33] Maia, I. A., Jordan, P., Cavalieri, A. V., Martini, E., Sasaki, K., and Silvestre, F. J., "Real-time reactive control of stochastic disturbances in forced turbulent jets," *Physical Review Fluids*, Vol. 6, No. 12, 2021, p. 123901.

[34] Audiffred, D. B., Cavalieri, A. V., Maia, I. A., Martini, E., and Jordan, P., "Reactive experimental control of turbulent jets," *Journal of Fluid Mechanics*, Vol. 994, 2024, p. A15.

[35] Audiffred, D., Mancinelli, M., Cavalieri, A., Martini, E., and Jordan, P., "Experimental Control of Jet Installation Noise," *30th AIAA/CEAS Aeroacoustics Conference (2024)*, 2024, p. 3314.

[36] Bres, G. A., Ham, F. E., Nichols, J. W., and Lele, S. K., "Unstructured large-eddy simulations of supersonic jets," *AIAA Journal*, Vol. 55, No. 4, 2017, pp. 1164–1184.

[37] Nielsen, E. J., and Kleb, W. L., "Efficient construction of discrete adjoint operators on unstructured grids using complex variables," *AIAA Journal*, Vol. 44, No. 4, 2006, pp. 827–836.

[38] Balay, S., Abhyankar, S., Adams, M. F., Benson, S., Brown, J., Brune, P., Buschelman, K., Constantinescu, E., Dalcin, L., Dener, A., et al., "PETSc/TAO Users Manual: Revision 3.18," Tech. rep., Argonne National Lab.(ANL), Argonne, IL (United States), 2022.

[39] Farghadan, A., Martini, E., and Towne, A., "Scalable resolvent analysis for three-dimensional flows," *Journal of Computational Physics*, Vol. 524, 2025, p. 113695.